Ferroelectrics, 483: 1–12, 2015

ISSN: 0015-0193 print / 1563-5112 online
DOI: 10.1080/00150193.2015.1058096

Taylor & Francis
Taylor & Francis Group

Materials Design of Visible-Light Ferroelectric Photovoltaics from First Principles

FENGGONG WANG,[1] ILYA GRINBERG,[1] LAI JIANG,[1] STEVE M. YOUNG,[1] PETER K. DAVIES,[2] AND ANDREW M. RAPPE[1,2,*]

[1]The Makineni Theoretical Laboratories, Department of Chemistry, University of Pennsylvania, Philadelphia, PA 19104-6323, USA
[2]Department of Materials Science and Engineering, University of Pennsylvania, Philadelphia, PA 19104-6272, USA

Further improvement of the power conversion efficiencies of conventional perovskite ferroelectric oxides has been strongly impeded by their wide band gaps. Here, we use several band gap engineering strategies to design low band gap ferroelectric materials from first principles. We show that polarization rotation is useful for reducing the band gaps of strongly distorted perovskites. A variety of visible-light ferroelectric solid solutions are designed by combining Zn substitution into $KNbO_3$ with polarization rotation. Alternatively, the band gaps can be reduced by the introduction of low-lying intermediate bands through Bi^{5+} substitution. With this strategy, two Bi^{5+}-containing visible-light ferroelectric solid solutions are designed, which exhibit comparable bulk photocurrent to that of prototypical ferroelectric oxides, but with lower photon energies, as evidenced by the shift current calculations.

Keywords Perovskite; ferroelectric; photovoltaic; shift current; band gap; polarization

I. Introduction

The efficient conversion of solar energy has been of great interest because solar energy is abundant, clean, and renewable, and is an ideal substitute for traditional fossil fuel energy resources [1]. Conventional solar cells are based on *p-n* junctions, and their power conversion efficiencies (PCEs) are limited by the Shockley-Queisser limit [2]. This is because the excited carriers are separated by the internal electric field at the *p-n* junction. Additionally, the need to form a *p-n* junction complicates the device fabrication. Ferroelectrics (FEs), possessing an intrinsic spontaneous polarization, provide an alternative way to separate excited carriers by the depolarizing field or by the bulk of the material [3, 4]. The photovoltaic effect due to carrier separation by the bulk of the material is called the bulk photovoltaic effect (BPVE), and can in principle occur in any polar material. In BPVE, the charge is excited to a coherent state that has an intrinsic momentum, and this leads to zero-bias

Received October 2, 2014; in final form April 14, 2015.
*Corresponding author. E-mail: rappe@sas.upenn.edu
Color versions of one or more figures in this article can be found online at www.tandfonline.com/gfer.

photocurrent, as shown by time dependent perturbation theory analysis [5–7]. The photovoltage generated by the BPVE can be above the material's band gap, potentially enabling higher PCEs beyond the Shockley-Queisser limit. Furthermore, ferroelectrics, especially ferroelectric oxides, can easily be synthesized using low-cost methods such as sol-gel and sputtering, as they are stable in a wide range of mechanical, chemical, and thermal conditions [8]. Therefore, recently ferroelectric ABO_3 perovskite oxides such as $BiFeO_3$ and $Pb(Zr_{1/2}Ti_{1/2})O_3$ (PZT) have been investigated in a variety of thin-film configurations [4, 9–19].

However, most conventional ferroelectric oxides have wide band gaps (E_g>2.7 eV for $BiFeO_3$, E_g>3.5 eV for PZT) and can only absorb 8–20% of the solar spectrum, which impedes further improvement of their PCEs. Therefore, theoretical design and engineering, and experimental demonstration of low band gap ferroelectric oxides have been the subject of many FE solar absorber studies [8, 20–36]. Recently, two visible-light oxides have been reported—a weakly ferroelectric nonperovskite ($KBiFe_2O_5$, $E_g = 1.6$ eV) [14], and the ferroelectric perovskite [(K,Ba)(Ni,Nb)$O_{3-\delta}$, $E_g = 1.39$ eV] [8]. Although the discovery of these visible-light absorbers has substantially advanced the study of ferroelectric photovoltaics, these materials still have some drawbacks. For example, $KBiFe_2O_5$ is only weakly ferroelectric and nonperovskite while the low gap of (K,Ba)(Ni,Nb)$O_{3-\delta}$ relies on a large concentration of oxygen vacancies. A nonperovskite structure gives rises to difficulties in integration into perovskite-based electronics, while oxygen vacancies are detrimental to polarization switching and can also trap carriers and increase both the radiative and nonradiative charge recombination rates. This motivates us to investigate alternative band-engineering strategies to lower the band gap E_g while preserving the ferroelectricity and to design new visible-light ferroelectric photovoltaics. Here, we propose strategies and design visible-light ferroelectric photovoltaics from first principles, and show that these newly designed materials can potentially be useful in photovoltaic energy conversion.

II. Methodology

First-principles density functional theory (DFT) calculations were performed using the pseudopotential plane-wave approach, as implemented in the QUANTUM-ESPRESSO code [37, 38]. Norm-conserving, optimized nonlocal pseudopotentials with a cutoff energy of 50 Ry, generated with the OPIUM package, were used to represent all the elements [39]. To accurately describe the structural properties of different systems, a variety of exchange-correlation functionals were used, including local density approximation (LDA), Perdew-Burke-Ernzerhof (PBE), and PBEsol generalized gradient approximation (GGA) [40–42]. The Monkhorst-Pack method was used to sample the Brillouin zone [43] and a dense enough k-point grid was adopted to guarantee convergence. The polarization was calculated following the Berry-phase approach [44, 45]. In order to avoid the unphysical delocalization of the strongly correlated d orbitals and to reduce the self-interaction error of standard DFT calculations, DFT+U and hybrid functional (HSE06 and PBE0) methods were also used [41, 46, 47]. For both HSE06 and PBE0, the exact exchange proportion is $\alpha = 0.25$, while in DFT+U the linear-response approach [48] was used to calculate the Hubbard U. The band gap was estimated using the single-particle Kohn-Sham eigenvalues, which is reasonable to compare to the fundamental band gap obtained by photoemission or electrochemical measurements [49]. To study the bulk photovoltaic

performance of some designed materials, we calculated the short-circuit shift current with linearly polarized light illumination using a recently developed approach [7].

III. Results and Discussions

A. Band Gap Reduction by Polarization Rotation

To design efficient solar energy converters, understanding the correlation between materials' structural properties (specifically the BO_6 octahedral tilting distortions and *B*-cation off-center displacements) and the electronic properties is highly desired [50, 51]. In this section, we demonstrate by first-principles calculations that the BO_6 octahedral distortions induced by the *B*-cation off-center displacements have a strong effect on band gap. We also propose a strategy to reduce the band gaps of perovskites while maintaining their polarizations by rhombohedral (*R*)-to-tetragonal (*T*) structural transitions with an accompanying polarization rotation from the (111) direction to the (100) direction [33]. Both the *R*- and *T*-phase perovskites are modeled using a five-atom unit cell after full structural relaxation. For some materials, this model is only hypothetical, but we use it on purpose to isolate the effects of *B*-cation displacements from the effects of other ABO_3 distortions.

As shown in Fig. 1 and Table 1, the band gap of the *R* perovskite phase is always larger than that of its *T* counterpart, irrespective of the composition. The GGA band gap difference between the *R* and *T* perovskites increases from 0.1 eV for $LaScO_3$ to 1.2 eV for WO_3, concurrently with the increase of the *B*-cation valence. This is because the antibonding O-*B* interaction is enhanced when the BO_6 octahedron distorts more significantly with phase transition from *T* to *R*, shifting the conduction band minimum (CBM) upward. This enhancement of the antibonding character becomes stronger as the valence of the *B*-cation increases and the *B*-O bonds become more covalent. The band gap change trend is quite robust and is confirmed by the HSE06 and PBE0 hybrid functional calculations, with the band gap differences changing by less than 0.15 eV when the functional is varied (Table 1). Furthermore, while the band gaps of perovskites are reduced by polarization rotation, the polarization magnitudes are largely preserved (Fig. 1). For more details, please see Ref. 33.

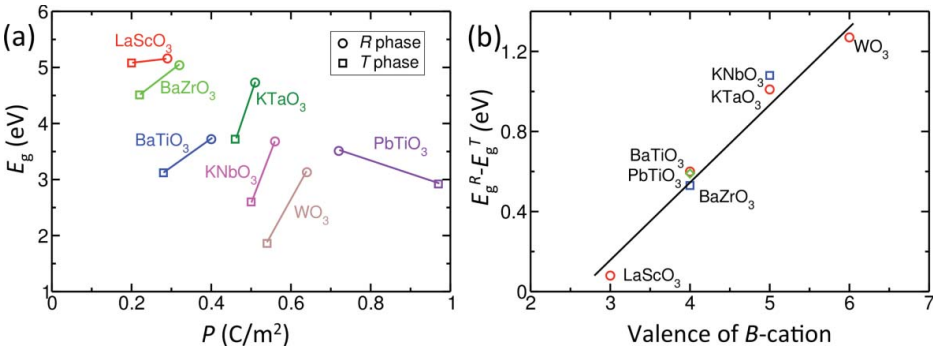

Figure 1. (a) The HSE06 band gap (eV) as a function of the polarization (C/m^2) in T and R perovskite oxides and (b) the band gap difference $E_g^R - E_g^T$ as a function of the valence of the *B*-cation. This figure is reproduced from Ref. 33.

Table 1
The band gap difference $E_g^R - E_g^T$ between rhombohedral and tetragonal perovskite oxides with various functionals

	$LaScO_3$	$BaTiO_3$	$BaZrO_3$	$PbTiO_3$	$KTaO_3$	$KNbO_3$	WO_3
GGA	0.13	0.56	0.59	0.68	0.97	1.01	1.18
HSE06	0.08	0.60	0.59	0.68	1.01	1.08	1.29
PBE0	0.07	0.60	0.56	0.65	1.02	1.10	1.30

This table is reproduced from Ref. 33.

B. Materials Design by Zn^{2+} Substitution and Polarization Rotation

Next, we design new visible-light ferroelectric photovoltaics by combining this polarization rotation strategy with Zn^{2+} substitution, as the local valence imbalance created by Zn substitution for a higher-valence *B*-cation in $KNbO_3$ gives rise to increased O 2*p*-Zn 3*d* repulsion and a higher valence band maximum (VBM) [34, 36]. We couple Zn substitution on the *B*-site with A_1^{2+} and A_2^{3+} substitution on the *A*-site ($A_1^{2+} = Pb^{2+}, Ba^{2+}, Sr^{2+}, A_2^{3+} = La^{3+}, Bi^{3+}$) of the parent $KNbO_3$ to make new solid solutions $(1-x)KNbO_3 - x(A_1^{2+\,1/2}, A_2^{3+\,1/2})(Zn_{1/2}, Nb_{1/2})O_3$ (KN-$A_1^{2+}A_2^{3+}$ZN) ($x = 0.25$). Fig. 2 shows the HSE06 band gaps of the KN-$A_1^{2+}A_2^{3+}$ZN solid solutions plotted as a function of the calculated Berry phase polarization. Clearly, the band gaps of all these newly designed solid solutions are 0.62–1.43 eV smaller than that of the parent rhombohedral phase $KNbO_3$. The band gap change trends with different *A*-site substitutions are very consistent for different functionals (Table 2), suggesting that they are accurately captured by our calculations.

The deficit of *B*-O bonding for the six O atoms around Zn because of the replacement of Nb^{5+} with a lower-valence Zn^{2+} ion must be compensated by the stronger *A*-O bonds with A_1^{2+} and A_2^{3+} cations substituting for the two K^+ ions. However, a build-up of

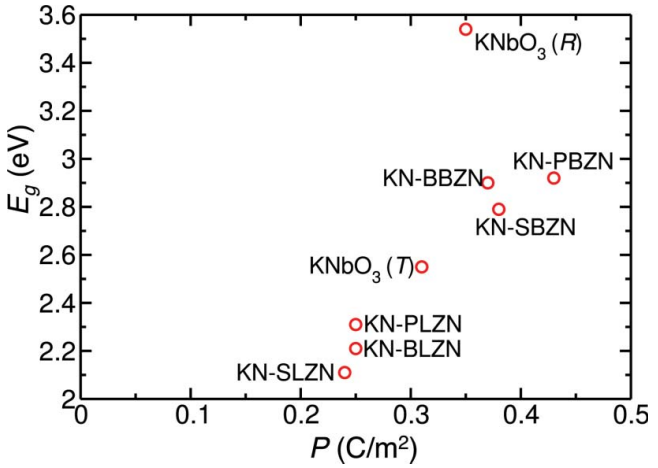

Figure 2. The HSE06 band gaps as a function of polarization for the designed solid solutions. Both rhombohedral (*R*) and tetragonal (*T*) $KNbO_3$ are shown for comparison. KN=$KNbO_3$, ZN="Zn, Nb", PL="Pb, La", PB="Pb, Bi", BL="Ba, La", BB="Ba, Bi", SL="Sr, La", SB="Sr, Bi". This figure is reproduced from Ref. 33.

Table 2
The band gaps E_g (eV) calculated with different methods and the polarization P (C/m^2) of various KN=$KNbO_3$-based solid solutions

	KN-BLZN	KN-SLZN	KN-PLZN	KN-BBZN	KN-SBZN	KN-PBZN	$KNbO_3$ (*T*)	$KNbO_3$ (*O*)	$KNbO_3$ (*R*)
E_g^{LDA}	1.05	0.93	1.10	1.60	1.56	1.75	1.40	1.63	2.24
$E_g^{\mathrm{LDA}+U}$	1.43	1.32	1.48	1.85	1.91	2.00	1.82	2.26	2.61
E_g^{HSE06}	2.21	2.11	2.31	2.90	2.79	2.92	2.55	3.15	3.54
P^{LDA}	0.25	0.24	0.25	0.37	0.38	0.43	0.31	—	0.35

The corresponding values of the parent $KNbO_3$ in tetragonal (*T*), orthorhombic (*O*), and rhombohedral (*R*) phases are also shown. KN=KNb, ZN="Zn, Nb", PL="Pb, La", PB="Pb, Bi", BL="Ba, La", BB="Ba, Bi", SL="Sr, La", SB="Sr, Bi"

This table is reproduced from Ref. 34.

nonbonding charge density on some O atoms is created because the compensation by the A_1^{2+} and A_2^{3+} cations is not enough at low $A_1^{2+}A_2^{3+}$ZN fractions. The nonbonding O charge densities push the energies of the O and Zn states up through their overlap with the Zn 3*d* states. This shifts the VBM up and lowers the E_g of the solid solutions with respect to the parent $KNbO_3$. The amount of the nonbonding O charge densities is different in KN-PBZN from that in KN-SLZN due to the different abilities of the Pb and Bi cations compared to the Sr and La ions to make large off-center displacements and covalent bonds. This gives rise to the differences in the band gap reduction in these two materials.

Because the band gaps of ZnO and other Zn-containing systems are underestimated even by HSE06 calculations [52], the band gaps of these newly designed solid solutions are still fairly high even though they have already been lowered significantly. Therefore, using in-plane compressive strains, we apply the polarization rotation strategy described above to these newly designed solid solutions as they all exhibit structures with polarization oriented along the [111] direction. As a result, the local polarization vector is rotated from [111] toward [001] by compressive strains (Fig. 3). We find that a 1% compressive strain reduces the HSE06 band gaps by 0.44–0.52 eV while a 2% strain reduces the gap by a further 0.10–0.20 eV. The further band gap lowering will lead to band gaps that are well within the visible light range. For more details, please see Ref. 34.

C. Materials Design by B-site Bi^{5+} Substitution

Materials with intermediate bands (IBs) have been suggested to be efficient solar cell candidates, and their PCEs can be comparable to that of the multijunction solar cells while avoiding the complex fabrication of multijunction or tandem device structures [53–56]. In this section, we reduce the band gaps of perovskites by introducing low-lying empty intermediate bands in the middle of the band gap through *B*-site Bi^{5+} substitution. Although previous studies have shown that a low-lying IB can arise in double perovskites Ba_2ReBiO_6 (*Re* = La, Ce, Nd, Sm, Eu, Gd, and Dy) and the substitution of only 5% Bi^{5+} into Ba_2InTaO_6 can reduce its band gap by 1.3 eV [57], none of these materials is ferroelectric. We design the visible-light absorbing perovskite ferroelectrics by Bi^{5+} substitution on the *B*-site of the ferroelectric perovskite.

For simplicity, we first test this strategy using the (1-*x*)$KNbO_3$-*x*$KBiO_3$ ($x = 0.125$, KNB) system even though the ionic radius mismatch between Nb^{5+} (0.64 Å) and Bi^{5+}

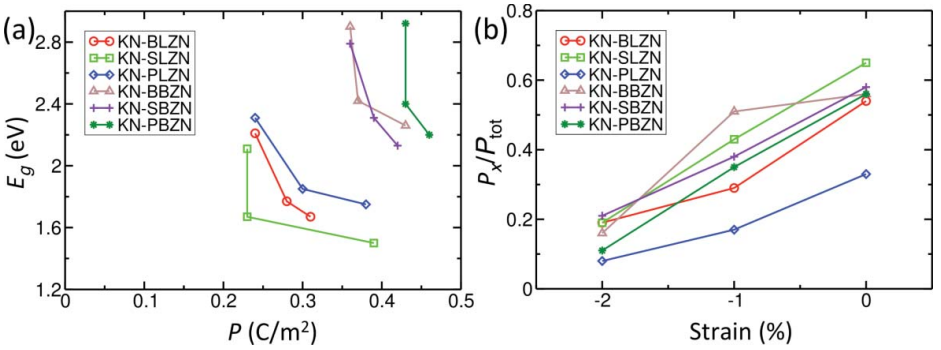

Figure 3. The (a) HSE06 band gap E_g as a function of the polarization P; and (b) ratio between the x-component of P and the total P (P_x/P_{tot}), of different $KNbO_3$-based solid solutions. In-plane compressive strain reduces E_g increases P, and reduces the x component of P. KN=$KNbO_3$, ZN="Zn, Nb", PL="Pb, La", PB="Pb, Bi", BL="Ba, La", BB="Ba, Bi", SL="Sr, La", SB="Sr, Bi". This figure is reproduced from Ref. 34.

(0.76 Å) is very large and $KBiO_3$ does not form a stable perovskite. We adopt the LDA, LDA+U, and PBEsol+U methods to verify the obtained trend in the band gap change, with $U \approx 3.9$ eV and 1.1 eV for Nb 4d and Bi 5d orbitals, respectively. We find that substitution of Bi^{5+} for Nb^{5+} induces an IB that is mostly composed of Bi 6s and O 2p orbitals, while the fundamental valence and conduction bands (VBs and CBs) do not change significantly. Upon substitution, the band gap decreases by 0.9–1.5 eV depending on the exchange-correlation functional while the polarization decreases from 0.4 C/m^2 to 0.25 C/m^2, confirming the validity of this strategy for creating visible-light absorbing perovskite ferroelectric photovoltaics.

We then apply this strategy to more feasible candidate solid solutions: (1-x) Pb_2InNbO_6-xBa_2InBiO_6 (PIN-BIB) and (1-x)Pb_2ScNbO_6-xBa_2ScBiO_6 (PSN-BSB) (x = 0.25). These systems should be more favorable candidates for experimental synthesis because the lattice mismatch between their end members is relatively small (PIN, 4.11 Å; BIB, 4.23 Å; PSN, 4.08 Å; and BSB, 4.18 Å). The LDA band structures and projected densities of states (PDOS) of both solid solutions are shown in Fig. 4. As in KNB, Bi^{5+} substitution introduces low-lying IBs composed of Bi 6s and O 2p orbitals in both PIN-

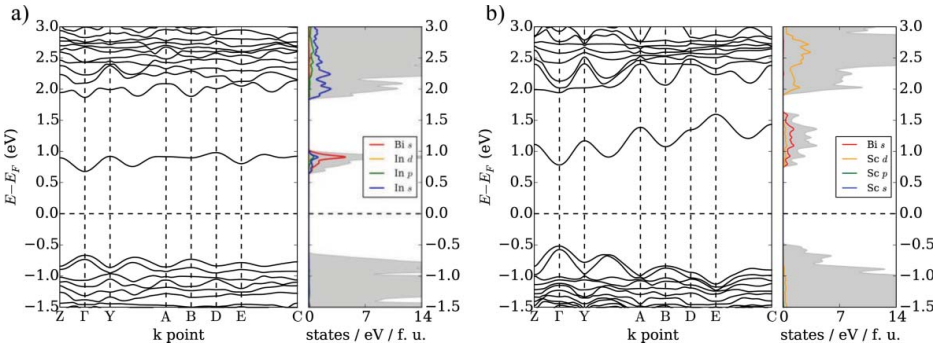

Figure 4. Band structures and PDOS for (a) PIN-BIB and (b) PSN-BSB; shaded areas indicate total DOS. This figure is reproduced from Ref. 35.

Table 3
Band gap E_g, polarization P, and lattice constants a, b and c of 0.75PIN-0.25BIB and 0.75PSN-0.25BSB

	E_g (eV)	P (C/m^2)	a (Å)	b (Å)	c (Å)
PIN-BIB	1.4	0.25 (0.07, 0.21, 0.11)	8.26	8.25	8.34
PSN-BSB	1.3	0.37 (0.11, 0.33, 0.11)	8.16	8.16	8.16

Numbers in parenthesis denote the three components of polarization.
This table is reproduced from Ref. 35.

BIB and PSN-BSB, reducing their band gaps significantly. The IB of PSN-BSB is more dispersive than that of PIN-BIB, suggesting that in PSN-BSB the excited electrons are more mobile with a lower effective mass. Both of the new solid solutions retain their polarizations and ferroelectric character (Table 3). Real-space wavefunction analysis suggests that the interaction between In *p* and O *p* is bonding in PIN-BIB, contributing significantly to the IB, whereas in PSN-BSB the *p*-*p* bonding interaction is negligible with only a tiny proportion of antibonding Sc *p*-O *p* interaction (Fig. 5). This gives rise to a higher energy at *E*-point in PSN-BSB, corresponding to a more dispersive IB. We corroborate this statement by using the tight-binding approach. For more details, please see Ref. 35.

D. Shift Current of the Bi^{5+}-Containing Solid Solutions

The bulk photovoltaic effect that is governed by the "shift current" mechanism arises when light shines onto noncentrosymmetric materials [58–61]. Shift current is a second-

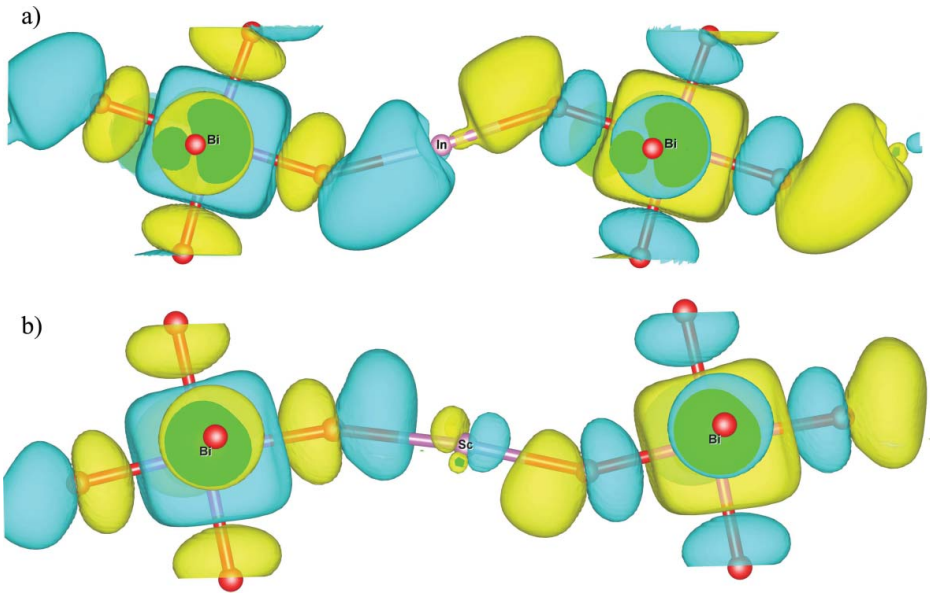

Figure 5. Real-space wavefunction for the IB at *E* point in (a) PIN-BIB and (b) PSN-BSB. This figure is reproduced from Ref. 35.

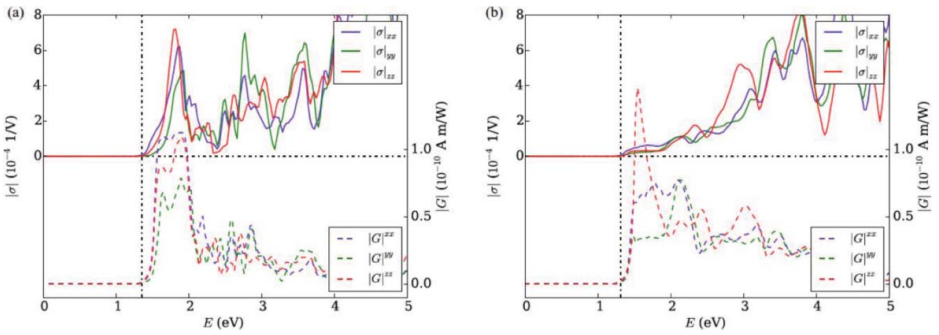

Figure 6. Total susceptibility (solid line) and Glass coefficient (dashed line) of (a) PIN-BIB and (b) PSN-BSB. For simplicity, we assume that both interactions are with the same monochromatic light (only σ_q^{rr}). This figure is reproduced from Ref. 35.

order nonlinear optical effect with the photocurrent quadratic in the electric field ($J_q = \sigma_q^{rs} E_r E_s$)) [7]. It does not rely on an externally engineered asymmetry or an internal depolarization field to separate charge. While our designed materials can be useful in conventional photovoltaics or by using the depolarization field at interfaces to separate charge, here we study the bulk shift current performance of the newly designed Bi^{5+}-containing materials by calculating their shift current susceptibilities σ_q^{rs} and the Glass coefficients ($G_q^{rr} = J_q(\omega)/Iw$) [4].

As expected, the photocurrent response thresholds of both Bi^{5+}-containing materials are located at relatively low photon energies—essentially at the theoretical band gap edge and well within the visible light range (Fig. 6). The shift current susceptibility of PSN-BSB increases continuously as the photon energy increases up to 4 eV, whereas that of PIN-BIB reaches maximum at a near-band-gap photon energy (1.9 eV). This is because the IB is more dispersive in PSN-BSB than in PIN-BIB. On the other hand, the Glass coefficients of both PIN-BIB and PSN-BSB are maximum at a near-band-gap photon energy and then decrease with higher incident photon energies. We attribute this to the relatively small absorption coefficients of PSN-BSB near the band gap compared to PIN-BIB. To evaluate the prospect of the Bi^{5+}-containing materials as solar energy converters, we compare them to the prototypical FE materials $PbTiO_3$, $BaTiO_3$, $BiFeO_3$ and $KNbO_3$. As shown in Table 4, the bulk shift current performance of both Bi^{5+}-containing

Table 4
The calculated largest shift current susceptibility σ and glass coefficient G of various materials (except for $BiFeO_3$) between the band gap E_g and 1 eV above it

	PIN-BIB	PSN-BSB	$PbTiO_3$	$BaTiO_3$	$BiFeO_3$	$KNbO_3$
σ (10^{-4} V^{-1})	7.2	1.7	3.9	1.4	0.9 (1.1)	11.1
G (10^{-10} Am/W)	1.1	1.4	1.2	0.2	0.05 (0.05)	0.3
E_g (eV)	1.4	1.3	3.4	3.2	2.7	3.1

For $BiFeO_3$, the numbers are calculated with the GGA+U method [62], and those in parentheses are the experimental values, both with a photon energy of 2.85 eV [7, 63].

This table is reproduced from Ref. 35.

materials are comparable to or stronger than that of the prototypical ferroelectric oxides, but their shift current onset photon energies are much lower. Therefore, they are promising candidates for applications using BPVE. For more details, please see Ref. 35.

IV. Conclusions

In summary, we propose band gap engineering strategies and design visible-light absorbing ferroelectric oxide photovoltaics from first principles. As a general strategy, polarization rotation is useful for reducing the band gap of perovskites with strong distortions. Combining polarization rotation and Zn doping into $KNbO_3$, a variety of ferroelectric oxides that possess band gaps well within the visible-light range are designed. New visible-light perovskite ferroelectrics are also designed by introducing low lying intermediate bands in the band gap through Bi^{5+} substitution at the *B* site. We show that the designed Bi^{5+}-containing solid solutions possess comparable or even stronger bulk photovoltaic performance with respect to the prototypical ferroelectric oxides. These may be useful for ferroelectric photovoltaic applications, potentially enabling higher PCEs beyond the Shockley-Queisser limit.

Funding

F. W. was supported by the Department of Energy under Grant No. DE-FG02-07ER46431. I. G. was supported by the Office of Naval Research under Grant No. N00014-12-1-1033. L. J. was supported by the Air Force Office of Scientific Research under Grant No. FA9550-10-1-0248. S. M. Y. was supported by the National Science Foundation under Grant No. DMR-1124696. P. K. D was supported by the Energy Commercialization Institute of BFTP. A. M. R. was supported by the Office of Naval Research under Grant No. N00014-11-1-0664. Computational support was provided by the High Performance Computing Modernization Office of the Department of Defense, and the National Energy Research Scientific Computing Center of the Department of Energy.

References

1. K. Maeda, K. Teramura, D. Lu, T. Takata, N. Saito, Y. Inoue, and K. Domen, Photocatalyst releasing hydrogen from water. *Nature*. **440**, 295 (2006).
2. W. Shockley, and H. J. Queisser, Detailed balance limit of efficiency of *p-n* junction solar cells. *J. Appl. Phys.* **32**, 510–519 (1961).
3. V. M. Fridkin, Bulk photovoltaic effect in noncentrosymmetric crystals. *Crystallog. Rep.* **46**, 654–658 (2001).
4. A. M. Glass, D. von der Linde, and T. J. Negran, High-voltage bulk photovoltaic effect and the photorefractive process in $LiNbO_3$. *Appl. Phys. Lett.* **25**, 233–235 (1974).
5. A. G. Chynoweth, Surface Space-charge layers in barium titanate. *Phys. Rev.* **102**, 705–714 (1956).
6. F. Nastos, and J. E. Sipe, Optical rectification and shift currents in GaAs and GaP response: below and above the band gap. *Phys. Rev. B.* **74**, 035201 (2006).
7. S. M. Young, and A. M. Rappe, First principles calculation of the shift current photovoltaic effect in ferroelectrics. *Phys. Rev. Lett.* **109**, 116601 (2012).
8. I. Grinberg, D. V. West, M. Torres, G. Gou, D. M. Stein, L. Wu, G. Chen, E. M. Gallo, A. R. Akbashev, P. K. Davies, J. E. Spanier, and A. M. Rappe, Perovskite oxides for visible-light-absorbing ferroelectric and photovoltaic materials. *Nature*. **503**, 509–512 (2013).

9. K. Nonaka, M. Akiyama, T. Hagio, and A. Takase, Effect of Pb/(Zr+Ti) Molar ratio on the photovoltaic properties of lead zirconate titanate ceramics. *J. Eur. Ceram. Soc.* **19**, 1143–1148 (1999).
10. T. Choi, S. Lee, Y. Choi, V. Kiryukhin, and S-W. Cheong, Switchable ferroelectric diode and photovoltaic effect in $BiFeO_3$. *Science*. **324**, 63–66 (2009).
11. S. Y. Yang, J. Seidel, S. J. Byrnes, P. Shafer, C-H. Yang, M. D. Rossel, P. Yu, Y-H. Chu, J. F. Scott, J. W. Ager, III, L. W. Martin, and R. Ramesh, Above-bandgap voltages from ferroelectric photovoltaic devices. *Nature Nanotech.* **5**, 143–147 (2010).
12. M. Alexe, and D. Hesse, Tip-enhanced photovoltaic effects in bismuth ferrite. *Nat. Commun.* **2**, 256 (2011).
13. J. Zhang, X. Su, M. Shen, Z. Dai, L. Zhang, X. He, W. Cheng, M. Cao, and G. Zou, Enlarging photovoltaic effect: combination of classic photoelectric and ferroelectric photovoltaic effects. *Sci. Rep.* **3**, 2109 (2013).
14. G. Zhang, H. Wu, G. Li, Q. Huang, C. Yang, F. Huang, F. Liao, and J. Lin, New high T_C multiferroics $KBiFe_2O_5$ with narrow band gap and promising photovoltaic effect. *Sci. Rep.* **3**, 1265 (2013).
15. J. You, Z. Hong, Y. Yang, Q. Chen, M. Cai, T-B. Song, C-C. Chen, S. Lu, Y. Liu, H. Zhou, and Y. Yang, Low-temperature solution-processed perovskite solar cells with high efficiency and flexibility. *ACS Nano*. **8**, 1674 (2014).
16. H. J. Snaith, Perovskites: the emergence of a new era for low-cost, high-efficiency solar cells. *J. Phys. Chem. Lett.* **4**, 3623–3630 (2013).
17. C. C. Stoumpos, C. D. Malliakas, and M. G. Kanatzidis, Semiconducting tin and lead iodide perovskites with organic cations: phase transitions, high mobilities, and near-infrared photoluminescent properties. *Inorg. Chem.* **52**, 9019–9038 (2013).
18. W. Ji, K. Yao, and Y. C. Liang, Bulk photovoltaic effect at visible wavelength in epitaxial ferroelectric $BiFeO_3$ thin films. *Adv. Mater.* **22**, 1763–1766 (2010).
19. M. Qin, K. Yao, and Y. C. Liang, High efficient photovoltaics in nanoscaled ferroelectric thin films. *Appl. Phys. Lett.* **93**, 122904 (2008).
20. D. Kan, V. Anbusathaiah, and I. Takeuchi, Chemical substitution-induced ferroelectric polarization rotation in $BiFeO_3$. *Adv. Mater.* **23**, 1765–1769 (2011).
21. J. W. Bennett, I. Grinberg, and A. M. Rappe, New highly polar semiconductor ferroelectrics through d^8 cation-O vacancy substitution into $PbTiO_3$: A theoretical study. *J. Am. Chem. Soc.* **130**, 17409–17412 (2008).
22. F. Wang, C. Di Valentin, and G. Pacchioni, Doping of WO_3 for photocatalytic water splitting: hints from density functional theory. *J. Phys. Chem. C.* **116**, 8901–8909 (2012).
23. R. Nechache, C. Harnagea, S. Licoccia, E. Traversa, A. Ruediger, A. Pigolet, and F. Rosei, Photovoltaic properties of Bi_2FeCrO_6 epitaxial thin films. *App. Phys. Lett.* **98**, 202902 (2011).
24. S. Takagi, V. R. Cooper, and D. J. Singh, Cooperative behavior of Zn cations in Bi-based perovskites: a comparison of $(Bi,Sr)_2ZnNbO_6$ and $(Bi,Sr)_2MgNbO_6$. *Phys. Rev. B.* 83–115130 (2011).
25. G. Y. Gou, J. W. Bennett, H. Takenaka, and A. M. Rappe, Post density functional theoretical studies of highly polar semiconductive $Pb(Ti_{1-x}Ni_x)O_{3-x}$ solid solutions: effects of cation arrangement on band gap. *Phys. Rev. B.* **83**, 205115 (2011).
26. Z. Li, Y. Shen, C. Yang, Y. Lei, Y. Guan, Y. Lin, D. Liu, and C-W. Nan, Significant enhancement in the visible light photocatalytic properties of $BiFeO_3$-graphene nanohybrids. *J. Mater. Chem. A.* **1**, 823–829 (2013).
27. Z. Zhang, P. Wu, L. Chen, J. Wang, Systematic variations in structural and electronic properties of $BiFeO_3$ by *A*-site substitution. *Appl. Phys. Lett.* **96**, 012905 (2010).
28. C-H. Yang, D. Kan, I. Takeuchi, V. Nagarajan, and J. Seidel, Doping $BiFeO_3$: approaches and enhanced functionality. *Phys. Chem. Chem. Phys.* **14**, 15953–15962 (2012).
29. R. F. Berger, and J. B. Neaton, Computational design of low-band-gap double perovskites. *Phys. Rev. B.* **86**, 165211 (2012).

30. W. S. Choi, M. F. Chisholm, D. J. Singh, T. Choi, J. E Jr.Jellison, and H. N. Lee, Wide bandgap tunability in complex transition metal oxides by site-specific substitution. *Nat. Commun.* **3**, 689 (2012).
31. F. Wang, C. Di Valentin, and G. Pacchioni, Rational band gap engineering of WO_3 photocatalyst for visible light water splitting. *ChemCatChem.* **4**, 476–478 (2012).
32. X. S. Xu, J. F. Ihlefeld, J. H. Lee, O. K. Ezekoye, E. Vlahos, R. Ramesh, V. Gopalan, X. Q. Pan, D. G. Schlom, and J. L. Musfeldt, Tunable band gap in $Bi(Fe_{1-x}Mn_x)O_3$ films. *Appl. Phys. Lett.* **96**, 192901 (2010).
33. F. Wang, I. Grinberg, and A. M. Rappe, Band gap engineering strategy via polarization rotation in perovskite ferroelectrics. *Appl. Phys. Lett.* **104**, 152903 (2014).
34. F. Wang, I. Grinberg, and A. M. Rappe, Semiconducting ferroelectric photovoltaics through Zn^{2+} doping into $KNbO_3$ and polarization rotation. *Phys. Rev. B.* **89**, 235105 (2014).
35. L. Jiang, I. Grinberg, F. Wang, S. M. Young, P. K. Davies, and A. M. Rappe, Semiconducting ferroelectric perovskite with intermediate bands via *B*-site Bi^{5+} doping. *Phys. Rev. B.* **90**, 075153 (2014).
36. T. Qi, I. Grinberg, and A. M. Rappe, Band-gap engineering via local environment in complex oxides. *Phys. Rev. B.* **83**, 224108 (2011).
37. P. Giannozzi, S. Baroni, N. Bonini, M. Calandra, R. Car, C. Cavazzoni, D. Ceresoli, G. L. Chiarotti, M. Cococcioni, I. Dabo, A. D. Corso, S. de Gironcoli, S. Fabris, G. Fratesi, R. Gebauer, U. Gerstmann, C. Gougoussis, A. Kokalj, M. Lazzeri, L. Martin-Samos, N. Marzari, F. Mauri, R. Mazzarello, S. Paolini, A. Pasquarello, L. Paulatto, C. Sbraccia, S. Scandolo, G. Sclauzero, A. P. Seitsonen, A. Smogunov, P. Umari, and R. M. Wentzcovitch, QUANTUM ESPRESSO: a modular and open-source software project for quantum simulations of materials. *J. Phys.: Condens. Matter.* **21**, 395502 (2009).
38. W. Kohn, and L. J. Sham, Self-consistent equations including exchange and correlation effects. *Phys. Rev.* **140**, A1133 (1965).
39. A. M. Rappe, K. M. Rabe, E. Kaxiras, and J. D. Joannopoulos, Optimized pseudopotentials. *Phys. Rev. B.* **41**, 1227 (1990).
40. J. P. Perdew, and A. Zunger, Self-interaction correction to density-functional approximations for many-electron systems. *Phys. Rev. B.* **23**, 5048 (1981).
41. J. P. Perdew, K. Burke, and M. Ernzerhof, Generalized gradient approximation made simple. *Phys. Rev. Lett.* **77**, 3865 (1996).
42. J. P. Perdew, A. Ruzsinszky, G. I. Csonka, O. A. Vydrov, G. W. Scuseria, L. A. Constantin, X. Zhou, and K. Burke, Restoring the density-gradient expansion for exchange in solids and surfaces. *Phys. Rev. Lett.* **100**, 136406 (2008).
43. H. J. Monkhorst, and J. D. Pack, Special points for Brillouin-zone integrations. *Phys. Rev. B.* **13**, 5188 (1976).
44. R. D. King-Smith, and D. Vanderbilt, Theory of polarization of crystalline solids. *Phys. Rev. B.* **47**, 1651 (1993).
45. R. Resta, Theory of the electric polarization in crystals. *Ferroelectrics*. **136**, 51–55 (1992).
46. K. A. Johnson, and N. W. Ashcroft, Corrections to density-functional theory band gaps. *Phys. Rev. B.* **58**, 15548 (1998).
47. J. Heyd, G. W. Scuseria, and M. Ernzerhof, Hybrid functionals based on a screened Coulomb potential. *J. Chem. Phys.* **118**, 8207–8215 (2003).
48. M. Cococcioni, and S. de Gironcoli, Linear response approach to the calculation of the effective interaction parameters in the LDA+*U* method. *Phys. Rev. B.* **71**, 035105 (2005).
49. F. Wang, C. Di Valentin, and G. Pacchioni, Electronic and structural properties of WO_3: a systematic hybrid DFT study. *J. Phys. Chem. C.* **115**, 8345–8353 (2011).
50. H. W. Eng, P. W. Barnes, B. M. Auer, and P. M. Woodward, Investigations of the electronic structure of d^0 transition metal oxides belonging to the perovskite family. *J. Solid State Chem.* **175**, 94–109 (2003).
51. A. Y. Borisevich, H. J. Chang, M. Huijben, M. P. Oxley, S. Okamoto, M. K. Niranjan, J. D. Burton, E. Y. Tsymbal, Y. H. Chu, P. Yu, R. Ramesh, S. V. Kalinin, and S. J. Pennycook,

Suppression of octahedral tilts and associated changes in electronic properties at epitaxial oxide heterostructure interfaces. *Phys. Rev. Lett.* **105**, 087204 (2010).
52. J. Wróbel, K. J. Kurzydlowski, K. Hummer, G. Kresse, and J. Piechota, Calculations of ZnO properties using the Heyd-Scuseria-Ernzerhof screened hybrid density functional. *Phys. Rev. B.* **80**, 155124 (2009).
53. A. Luque, and A. Martí, Increasing the efficiency of ideal solar cells by photon induced transitions at intermediate levels. *Phys. Rev. Lett.* **78**, 5014–5017 (1997).
54. A. Martí, E. Antolín, C. R. Stanley, C. D. Farmer, N. López, P. Díaz, E. Cánovas, P. G. Linares, and A. Luque, Production of photocurrent due to intermediate-to-conduction-band transition: a demonstration of a key operating principles of the intermediate-band solar cell. *Phys. Rev. Lett.* **97**, 247701 (2006).
55. A. Luque, A. Martí, and C. Stanley, Understanding intermediate-band solar cells. *Nat. Photon.* **6**, 146–152 (2012).
56. N. López, L. A. Reichertz, K. M. Yu, K. Campman, and W. Walukiewicz, Engineering the electronic band structure for multiband solar cells. *Phys. Rev. Lett.* **106**, 028701 (2011).
57. T. Hatakeyama, S. Takeda, F. Ishikawa, A. Ohmura, A. Kakayama, Y. Yamada, A. Matsushita, and J. Yea, Photocatalytic activities of Ba_2RBiO_6 (R=La, Ce, Nd, Sm, Eu, Gd, Dy) under visible light irradiation J. *Ceram. Soc. J.* **118**, 91–95 (2010).
58. G. Dalba, Y. Soldo, F. Rocca, V. M. Fridkin, and P. H. Sainctavit, Giant bulk photovoltaic effect under linearly polarized X-ray synchrotron radiation. *Phys. Rev. Lett.* **74**, 988 (1995).
59. R. von Baltz, and W. Kraut, Theory of the bulk photovoltaic effect in pure crystals. *Phys. Rev. B.* **23**, 5590–5596 (1981).
60. K. Tonooka, P. Poosanaas, and K. Uchino, Mechanism of the bulk photovoltaic effect in ferroelectrics. Proc. SPIE **3324**, 224–232 (1998).
61. B. I. Sturman, and V. M. Fridkin, Principles of the microscopic theory. In: G. W. Taylor, eds. *Ferroelectricity and Related Phenomena*. New York: Gordon and Breach; (1992).
62. S. M. Young, F. Zheng, and A. M. Rappe, First-principles calculation of the bulk photovoltaic effect in bismuth ferrite. *Phys. Rev. Lett.* **109**, 236601 (2012).
63. W. Ji, K. Yao, and Y. C. Liang, Evidence of bulk photovoltaic effect and large tensor coefficient in ferroelectric $BiFeO_3$ thin films. *Phys. Rev. B.* **84**, 094115 (2011).